



Constructing nanoporous Ni foam current collectors for stable lithium metal anodes

Shikun Liu^a, Hongming Zhang^a, Xiaoxu Liu^b, Yu Yang^a, Caixia Chi^a, Shen Wang^a, Junying Xue^a, Tingting Hao^a, Jiupeng Zhao^{a,*}, Yao Li^{c,*}

^aSchool of Chemistry and Chemical Engineering, Harbin Institute of Technology, Harbin 150001, Heilongjiang, China

^bSchool of Material Science and Engineering, Shaanxi Key Laboratory of Green Preparation and Functionalization for Inorganic Materials, Shaanxi University of Science and Technology, Xi'an 710021, Shaanxi, China

^cCenter for Composite Materials and Structure, Harbin Institute of Technology, Harbin 150001, Heilongjiang, China

ARTICLE INFO

Article history:

Received 3 September 2020

Accepted 8 September 2020

Available online 20 September 2020

Keywords:

Lithium metal anodes

Nanopores

Current collector

Ni foam

Stable cycling lifespan

ABSTRACT

Lithium metal, as the most ideal anode material for high energy density batteries, has been researched for several decades. However, the dendrite formation and large volume change during repetitive lithium plating/stripping lead to a serious safety issue and impede the practical application of lithium metal anode. Herein, a nanoporous Ni foam current collector with high surface area and surface flaws is constructed via a facile oxidation–reduction method. The inherent macropore structure of Ni foam can partly accommodate the volume variation during Li plating/stripping. The well-distributed nanopores on the skeleton of Ni foam can effectively reduce the local current density, regulate the uniform lithium nucleation and deposition with homogenous distribution of Li⁺ flux. Moreover, the surface flaws induce the formation of ring Li structures at initial nucleation/deposition processes and concave Li metal spontaneously formed based on the ring Li structures during cycling, which can direct the even Li plating/stripping. Therefore, highly stable Coulombic efficiency is achieved at 1 mA cm⁻² for 200 cycles. The symmetrical cell, based on the nanoporous Ni foam current collector, presents long lifespans of 1200 and 700 h respectively at different current densities of 0.5 and 1 mA cm⁻² without short circuit. In addition, the LiFePO₄ full cell, with the Li metal anode based on the nanoporous Ni foam current collector, shows excellent cycling performance at 1C for 300 cycles and rate performance.

© 2020 Science Press and Dalian Institute of Chemical Physics, Chinese Academy of Sciences. Published by ELSEVIER B.V. and Science Press. All rights reserved.

1. Introduction

Lithium-ion batteries (LIBs) have promoted the wide applications and developments of various electronic devices, such as mobile phones, laptops, drones and robots [1–3]. For the moment, the low energy density (200–250 Wh kg⁻¹) of commercial LIBs, using the graphite (372 mAh g⁻¹) as anode, cannot meet the requirements for lightweight and longer working hours of electronic devices, especially for the tremendous increase of electric vehicles [4,5]. This highlights the urgent need for next generation batteries with high energy density. Recently, Li metal anodes (LMAs) are revived due to its high theoretical capacity of 3860 mAh g⁻¹, low reduction potential (–3.04 V vs. standard hydrogen electrode) and low density (0.53 g cm⁻³) [6–8]. However, the practical utilization of LMAs is still hindered by several formidable

challenges, e.g., formation and growth of Li dendrite, large volume change, formation of dead Li, low Coulombic efficiency (CE) and internal short circuit [9–11]. Among them, dendrite growth and infinite volume expansion are the two main limitations of LMAs [3,12]. The continuous Li dendrite growth can seemingly penetrate the separator and contact the cathode, resulting in short circuit of a working cell and safety risk [9,13]. Moreover, the dead Li will be formed if the dissolution of Li metal originates from the root of Li dendrite [14–16]. Meanwhile, the volume change of LMAs is infinite during repeated Li plating/stripping owing to its hostless nature, which fractures the fragile solid electrolyte interphase (SEI) film, causing the touch between fresh Li metal and electrolyte, accelerating the consume of Li metal and electrolyte and eventually leading to the low CE and poor cycle life [2,17,18].

Considerable efforts have been conducted to tackle the above mentioned problems. One approach is to adjust the electrolyte composition via adding additives to construct a stable SEI layer on LMAs, such as fluoroethylene carbonate (FEC) [19], vinylene

* Corresponding authors.

E-mail addresses: jpzhaoh@hit.edu.cn (J. Zhao), yaoli@hit.edu.cn (Y. Li).

carbonate (VC) [20], AlCl_3 [21], and LiNO_3 [22]. Although this method is simple and stabilizes the LMAs to some extent, the effect of additives is not permanent due to the depletion of those additives during repetitive charge/discharge cycling [23]. Alternatively, the LMAs can be coated with an artificial passivation layer to effectively stabilize the LMAs before assembling cells, such as hollow carbon nanosphere layer [24], Li_3PO_4 layer [25], and LiF film [26]. However, the artificial SEI layer has not been robust enough to conquer the unavoidable volume change of LMAs during plating/stripping process. Moreover, the deposited Li with high capacity deteriorate the strength of artificial SEI layer and generate cracks in the interface, causing a side reaction between Li metal and electrolyte, thus resulting in low CE and poor cycle life [27]. Another approach is to modify the separator structure to avoid Li dendrite penetration [28–30], which cannot solve the problems of the formation of dendrite and dead Li thoroughly. Recently, three-dimensional (3D) conductive frameworks with high surface areas have been developed to accommodate the Li deposition, including 3D porous Cu host [12,31–35], 3D porous Ni host [36], nitrogen-doped carbon nanofiber [37], and nitrogen-doped graphitic carbon foams [38]. Based on the Sand's time, in other words the initial time of dendrite growth, these current collectors possessing large surface area can reduce local current density and homogenize Li^+ flux distribution, hence delay the dendrite growth [14,39]. Furthermore, the use of these hosts effectively accommodates the deposited Li and alleviates volume change. Commercially available Ni foam has been extensively employed as current collectors or support frameworks for various applications in different fields, such as batteries [40], supercapacitors [41], and electrocatalysis [42]. Comparing to the Cu based host, the Ni based host has smaller nucleation overpotential for Li deposition, implying smaller Li nucleation barrier on Ni than that on Cu [43]. The interconnected porous structure, which can accommodate the volume change of LMAs [11,44], and low cost of Ni foam makes it ideal for 3D Li host. However, dendritic Li trends to be formed on the metallic skeletons of Ni foam due to the uneven distribution of Li^+ flux (Scheme 1a). Hence, Ni foam needs to be further processed to make it become a desirable current collector for LMAs. Besides, researchers have reported that the “well-like” holes constructed on Li foil anode itself can direct Li plating/stripping process, then the modified Li foil anode exhibits low overpotential and stable cycling performance [45,46].

Herein, we developed a facile oxidation–reduction strategy to fabricate nanoporous Ni foam (NPNF) with larger surface area than pure Ni foam (NF), hence, the NPNF current collector is able to reduce the local current density to a greater extent. Besides, the well-distributed nanopores can guide the homogenous distribution of Li^+ flux and uniform nucleus of Li at a small nucleation overpotential (Scheme 1b). Moreover, the flaws on the NPNF can induce

the formation of ring structures at the initial Li nucleation/deposition processes, then some concave structures spontaneously formed based on the ring structures on the Li@NPNF anode during cycling, which can guide Li plating/stripping. As a result, LMAs with NPNF current collector reveals apparently reduced polarization, and excellent lifespan with a high CE (98.7%) even after 200 cycles at 1 mA cm^{-2} . The symmetric $\text{Li}|\text{Li@NPNF}$ cell exhibits a long cycling life up to 1200 h at 0.5 mA cm^{-2} and 700 h at 1 mA cm^{-2} . When assembled with a LiFePO_4 cathode, the full cell combined with the NPNF current collector shows better rate performance and high capacity retention of 93% after 300 cycles at 1C, comparing to the case of the NF current collector with a much lower capacity retention of 78.9% after 150 cycles, even cell failure after 190 cycles.

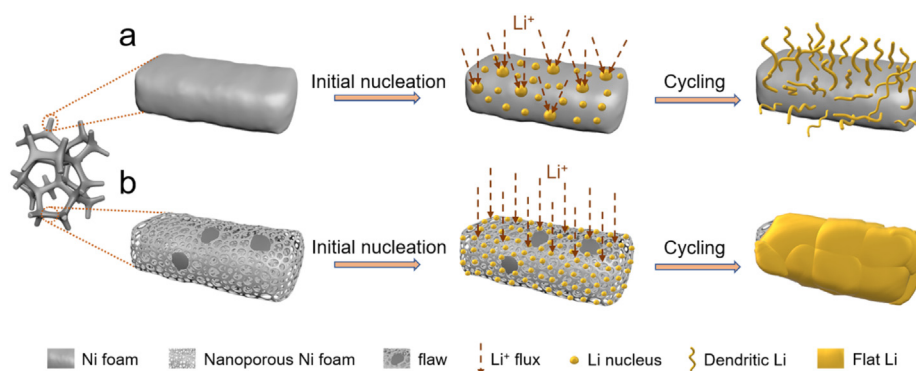
2. Experimental

2.1. Fabrication of the nanoporous Ni foam

Commercial Ni foams were first cut into disks with diameter of 12 mm and washed with absolute alcohol for three times to remove the surface impurities in a sonication bath, then dried in an oven at 60°C without any other treatments. Afterwards, the prepared Ni foam disks were transferred into a tube furnace and oxidized at 700°C for 8 h in ambient environment. After the tube furnace cooling down, the oxidized Ni foams were reduced at 500°C for 5 h in a mixed atmosphere with hydrogen and argon ($\text{H}_2:\text{Ar} = 5:95 \text{ vol\%}$) to obtain the final nanoporous Ni foam current collector for LMAs.

2.2. Material characterization

The crystal structures of pure Ni foam, oxidized Ni foam and nanoporous Ni foam were characterized by X-ray diffraction (XRD) using a Rigaku D/max-rB X-ray diffractometer with $\text{Cu } K_\alpha$ ($\lambda = 0.15418 \text{ nm}$) incident radiation. The BET surface area and pore-size distribution were evaluated using the nitrogen adsorption/desorption technique (3H-2000PS1) and mercury intrusion technique (AutoPore IV 9510), respectively. The morphology and nanostructures of these three samples were analyzed by a scanning electron microscopy (SEM, SUPRA-55 SAPPHERE). For the observation of the morphology of deposited Li on NF and NPNF current collectors, the cycled cells were disassembled in an Ar-filled glovebox, the LMAs were then washed with dimethyl carbonate (DMC) to remove residual electrolyte and dried in the glovebox at room temperature before characterization. The prepared LMAs were loaded in a sealed container filled with Ar and rapidly transferred to the SEM vacuum chamber avoiding prolonged exposure



Scheme 1. Schematics of Li metal deposition behavior on different current collectors of (a) pure Ni foam current collector and (b) nanoporous Ni foam current collector.

to air. Elemental mapping of oxidized Ni foam was carried out before and after reduction by SEM with energy dispersive X-ray spectrometry (EDS).

2.3. Electrochemical measurements

To measure the electrochemical performances of LMAs, CR2032 coin cells were installed in an Ar-filled glove box (H_2O and O_2 contents <0.1 ppm) using NF or NPNF current collector as the working electrode, metallic Li foil as the counter/reference electrode, polypropylene (PP) film (Celgard 2400) as the separator, and 1 M lithium bis(trifluoromethanesulfonyl)imide (LiTFSI) in 1,3-dioxolane (DOL) and 1,2-dimethoxyethane (DME) ($v:v = 1:1$, 60 μL) with 1 wt% LiNO_3 as the electrolyte. The assembled coin cells were tested using a channels battery analyzer (Neware CT-3008). Before the formal measure, coin cells were firstly cycled at 0.05 mA for five times between 0 and 1 V vs. Li/Li^+ to remove the surface contaminations of current collectors and to stabilize the SEI layer. To assess CE, a fixed amount of 1 mAh cm^{-2} of Li was electrochemically deposited on the current collector from Li foil counter electrode and then was stripped away by charging to 1 V vs. Li/Li^+ at 1 mA cm^{-2} . Electrochemical impedance spectrum (EIS) test was recorded with a frequency ranging from 100 kHz to 10 mHz and a AC signal of 5 mV in amplitude as the perturbation using a CHI660E electrochemical workstation (Shanghai Chenhua, China). To test the cycling stability and rate performance of symmetric cell, 4 mAh cm^{-2} of Li was firstly deposited on the NF or the NPNF current collector to form the Li@NF anode or the Li@NPNF anode at a current density of 0.5 mA cm^{-2} . For cycling stability measurement, the $\text{Li}||\text{Li@NF}$ or the $\text{Li}||\text{Li@NPNF}$ cells were charged/discharged at 0.5 mA cm^{-2} for 2 h of each cycle or at 1 mA cm^{-2} for 1 h of each cycle. For the rate performance measurement, the symmetric cells were charged/discharged at different current densities with a fixed capacity of 1 mAh cm^{-2} .

The full cells were assembled to compare the electrochemical performances of the Li@NF anode and Li@NPNF anode. Before using the Li@NF or Li@NPNF as the anode, they were washed with DMC and dried in the glovebox at room temperature. Commercial LiFePO_4 was used as the cathode material in the full cells. LiFePO_4 power, polyvinylidene difluoride (PVDF) and Super P (mass ratio: 8:1:1) were mixed in N-methyl-2-pyrrolidone (NMP) to form the cathode slurry, which was casted on Al foil current collector and dried under vacuum atmosphere at 120 $^\circ\text{C}$ for 12 h. Both low mass loading (~ 2.0 mg cm^{-2}) and high mass loading (~ 11.4 mg cm^{-2}) of LiFePO_4 were fabricated. The prepared cathode was cut into round disk with a diameter of 12 mm. The full cell was charged/discharged at 2.8–4.0 V vs. Li/Li^+ at 1C (1C = 172 mA g^{-1}) for cycling stability test or at various current for rate performance test.

3. Results and discussion

Fig. 1(a, b, e) shows the surface morphology of the Ni foam and its appearance changes after oxidation and reduction successively. Fig. S1 exhibits the low resolution SEM images of the samples. It can be observed that the surface morphology of the Ni foam becomes very rough after heat treatment in the air (Fig. 1b) and the color is transformed into dark green (inset in Fig. 1b), which indicates that there is a layer of nickel oxide (NiO) formed on the surface of the Ni foam. Element mapping of cross-sectional SEM image of the oxidized Ni foam (Fig. 1c) and XRD patterns (red line in Fig. 1d) further confirm the presence of NiO . The oxidized Ni foam was then annealed in the mixed gas of H_2 and Ar to fabricate NPNF current collector, as showed in Fig. 1(e). It is noted that nanopores with size ranging between 200 and 800 nm are formed inside the nickel skeleton (Fig. 1f), which can greatly increase the surface

area of NPNF current collector, decrease the local current density and induce the uniform nucleation of Li, thus prolong the time of Li dendrite formation. The BET surface area of NPNF was evaluated to be 1.83 $\text{m}^2 \text{g}^{-1}$, twice larger than that of NF (0.81 $\text{m}^2 \text{g}^{-1}$), using the nitrogen adsorption/desorption technique (Fig. S2a). The mercury intrusion technique was used to compare the pore size distributions of NF and NPNF, as shown in Fig. S2(b). It can be observed that the size of the nanopores in NPNF is mainly concentrated around 435 nm. The porosity and total pore volume of NPNF are respective 82.1% and 1.29 $\text{cm}^3 \text{g}^{-1}$, while the total pore volume of NF is only 0.9 $\text{cm}^3 \text{g}^{-1}$, less than 70% of that of NPNF. XRD profiles (Fig. 1d) demonstrate that the oxidized Ni foam has been reduced completely. The element mapping of NPNF current collector (Fig. 1f) also exhibits the disappearance of oxygen, both on the surface and inside the bulk of nickel skeleton, after reducing of oxidized Ni foam. Hence, the conductivity will not decrease when the NF is changed into the NPNF current collector (Fig. S3).

The Li plating/stripping behavior on the NPNF current collector was investigated to observe the morphology evolution of Li metal via ex-situ SEM (Fig. 2). It can be seen that when the amount of deposited Li on the NPNF current collector is 1 mAh cm^{-2} , the morphology of Li metal is large grain structure (Fig. 2b). It can be noted that some Li grains present irregularly concave shape (Fig. 2b, yellow line parts), which can guide Li metal to preferentially deposit in the interior of concave Li grains during the subsequent Li deposition [45,46]. With increasing the amount of Li metal on the NPNF current collector, the concave Li grains eventually are filled with Li metal and all the Li grains gradually grow up and contact each other to form an even and dense surface (Fig. 2c, d). The Li metal can also be stripped reversibly from the NPNF current collector. As shown in Fig. 2(e–g), the Li metal is gradually stripped from the NPNF current collector and is completely stripped after charging to 1 V. It is noted that the concave Li structures occur when the amount of stripped Li is 2 mAh cm^{-2} (Fig. 2e), which can guide Li metal to preferentially strip along the rims of the concave shape [45]. Furthermore, the structural stability of the nanopores and high surface area of the NPNF current collector can be kept after Li stripping (Fig. 2g). After repeated cycles, the surface of the Li@NPNF anode still remains flat without occurrence of protruding Li dendrites (Fig. 2h). The flat surface of Li@NPNF anode may result from the large surface area of the current collector due to the nanopores, which reduces the local current density, and the formation of concave Li metal which directs Li metal to plate and strip more uniformly.

The formation of the concave Li grains, during Li plating process, may be attributed to the basin-like flaws on the surface of NPNF current collector, as shown in Fig. 2(a). The surface flaws induce uneven electrostatic field over a small range, that is the charge density at the edge is higher than that at the center of the basin-like flaws according to the classical electromagnetism principles [47,48]. Hence the Li metal will preferentially nucleate and grow around the flaws. SEM images in Fig. 3(a) further demonstrate this hypothesis. It can be seen that the Li deposits present ring structures, precursors of the concave structures, at the initial nucleation process, with a very low Li capacity of 0.05 mAh cm^{-2} . The ring Li structures will have a guiding function for the formation of concave Li grains. Fig. 3(b) shows that the Li particles would preferentially deposit in the interior of concave structures. Fig. 3(c, d) show that the concave and spherical Li deposits are coexisting at low Li capacity of 0.2 mAh cm^{-2} . The schematics in Fig. S4 shows the formation processes of the concave and spherical Li grains. It is noted that the partial surface flaws have a negligible effect on the uniform distribution of current density for the whole NPNF current collector.

The morphology evolution of Li metal deposited on the NF current collector was also investigated via ex-situ SEM during Li plat-

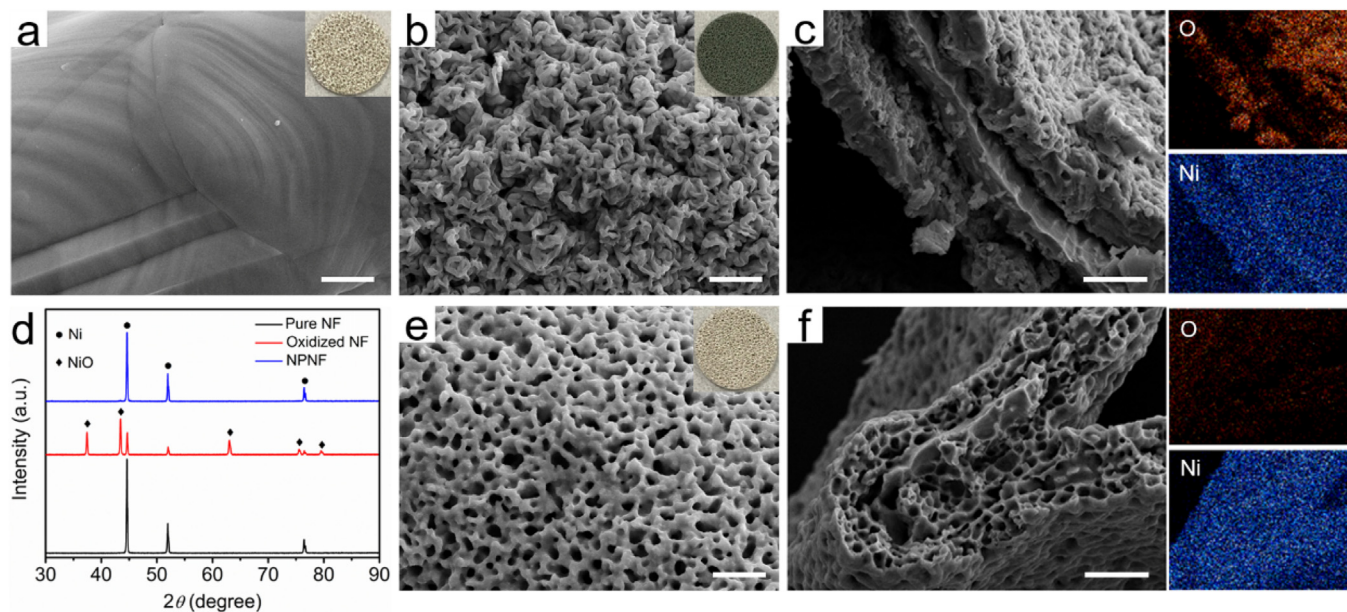


Fig. 1. SEM images of (a) NF, (b) oxidized NF and (e) NPNF. Insets are the corresponding digital photographs. Element mapping of cross-sectional SEM images of (c) oxidized NF and (f) NPNF. Scale bars: (a, b, e) 2 μm , (c, f) 5 μm . (d) XRD patterns of NF, oxidized NF and NPNF.

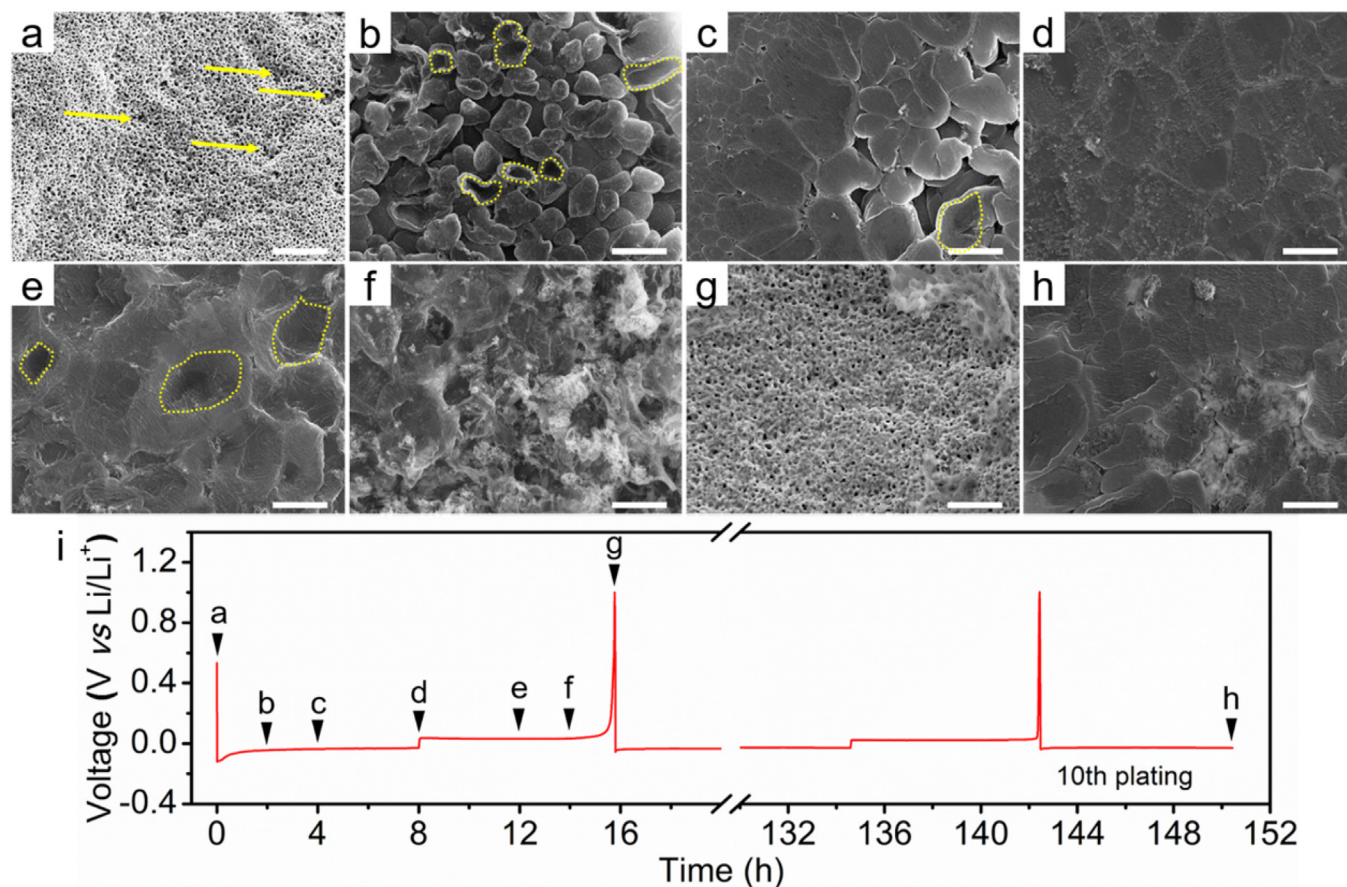


Fig. 2. Morphology of Li@NPNF anodes during plating/stripping for different capacities of Li metal. SEM images of (a) pristine NPNF current collector without Li metal and after plating (b) 1 mAh cm^{-2} , (c) 2 mAh cm^{-2} and (d) 4 mAh cm^{-2} of Li metal on the NPNF current collector; SEM images of Li@NPNF anodes after stripping (e) 2 mAh cm^{-2} , (f) 3 mAh cm^{-2} and (g) 4 mAh cm^{-2} (that is, charged to 1 V) of Li metal. (h) SEM image of the Li@NPNF anode after 10th plating. Scale bars, 10 μm . Galvanostatic discharge/charge voltage profile (i) indicates the Li plating/stripping states (a–h) at 0.5 mA cm^{-2} .

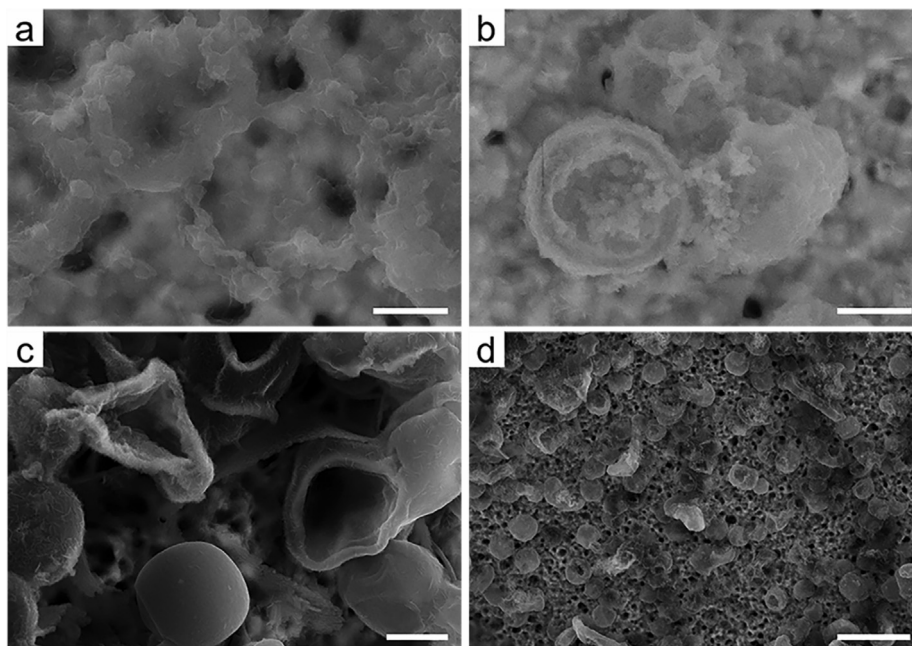


Fig. 3. SEM images of Li deposits on NPNF current collector with the Li capacity of (a) 0.05 mAh cm^{-2} , (b) 0.1 mAh cm^{-2} and (c, d) 0.2 mAh cm^{-2} . Scale bars: (a, b) $1 \mu\text{m}$, (c) $2 \mu\text{m}$, (d) $10 \mu\text{m}$.

ing/stripping (Fig. S5). Compared to the Li@NPNF anode, the Li@NF anode shows a dendrite morphology in the whole plating/stripping process. It can be seen that dead Li has been formed when the charging voltage reaches to 1 V (Fig. S5g). The dead Li can also be distinctly observed after the 10th Li plating (Fig. S5h). The less plating/stripping time (149.1 h, Fig. S5i) than that of Li@NPNF anode (150.5 h, Fig. 2i), that is about 0.15 h less per stripping cycle on average, further indicates the formation of the dead Li that reduces the CE. The cross-sectional morphology evolutions of both Li@NPNF anode and Li@NF anode were further investigated to compare the performances of the NPNF and NF current collectors during Li plating/stripping, as shown in Figs. S6 and S7. For the Li@NPNF anode, the deposited Li metals are main grain and flat structures during Li plating process (Fig. S6a–c), while for the Li@NF anode the Li dendrite exist (Fig. S7a–c). During Li stripping process, the size of the Li dendrite gradually reduces and eventually becomes dead Li (Fig. S7d–f). By contrast, the Li@NPNF anode shows more evenly stripping, without obvious dead Li except the remaining SEI layers (Fig. S6d–f). After the 10th plating, the Li@NPNF anode still exhibits flat structure (Fig. S6g), while the Li@NF anode presents dead Li and dendritic Li structures (Fig. S7g). The magnified SEM images of Figs. S(6h) and S(7h) further show the flat structure of the Li@NPNF anode and the obvious dead Li on the Li@NF anode.

As shown in Figs. S6(h) and S7(h), because the Li will firstly deposit on the conductive upper surface, the pores cannot be fully used to accommodate the deposited Li. This problem can be solved by using melt-infusion method. Chi et al. have demonstrated that the NF can be filled with Li metal via melt-infusion method at $\sim 400 \text{ }^\circ\text{C}$ [44]. If all pores are full of Li in the NPNF, it can provide more capacity than NF or it can reduce the anode volume at the same capacity by using thinner current collector due to the larger total pore volume of NPNF ($1.29 \text{ cm}^3 \text{ g}^{-1}$) than that of NF ($0.9 \text{ cm}^3 \text{ g}^{-1}$). Based on the density and theoretical capacity of Li metal, a gram of NPNF or NF can respectively accommodate 0.68 or 0.48 g Li and the specific capacities of the Li@NPNF anode and the Li@NF anode are respective 1562 and 1252 mAh g^{-1} . However, this work mainly focused on the properties of the current collector itself and its influence on the nucleation/deposition of Li.

To evaluate the electrochemical cycling stability of the NPNF current collector, CE test was carried out at 1 mA cm^{-2} with a capacity of 1 mAh cm^{-2} for the both NF and NPNF current collectors, as shown in Fig. 4(a). The amount of the stripped Li capacity was controlled via a charging cut-off voltage at 1 V vs. Li/Li^+ . Fig. S8(a, b) shows the charging and discharging profiles of the both current collectors at different cycles. The CE of NPNF current collector shows a good stability, remaining fairly stable for 200 cycles and exhibiting a high CE of 98.7% even after 200 cycles. The stable CE indicates the uniform Li plating and stripping behavior. However, for the NF current collector, the CE shows a vast drop from the 54th cycle (96.3%) to 77th cycle (84.3%) and irregularly fluctuates in the subsequent cycles, which could be ascribed to the continuous growth/corrosion of Li dendrites [38]. The CE of NF current collector is only 75.6% at 200th cycle. The advantage of NPNF current collector was also verified by the nucleation overpotential which is the difference between the dip voltage and the stable voltage plateau. Fig. 4(b) shows the first charging/discharging profiles of NF and NPNF current collectors at 1 mA cm^{-2} . It can be observed that the NPNF current collector has a smaller nucleation overpotential of 106.7 mV than that of the NF current collector (266.6 mV). The lower nucleation overpotential for the NPNF current collector indicates that the high surface area significantly decreases the practical current density for the deposition of Li metal and then contributes to the uniformity of initial nucleation.

The corresponding voltage hysteresis, which is the gap between the voltages of Li plating and stripping, further confirms the superiority of the NPNF current collector. Voltage hysteresis is mainly controlled by the current density, charge transfer resistance and interfacial properties [36]. Fig. 4(c) displays that the NF current collector has a high and fluctuating voltage hysteresis, while the voltage hysteresis of the NPNF current collector is lower and more stable. The result should be ascribed to the larger surface area of the NPNF current collector, which can lower the practical current density and provide a larger interface between the NPNF current collector and electrolyte to reduce the charge transfer resistance during cycling compared with the NF current collector. Fig. S8(c, d) shows the enlarged voltage profiles of the both current collectors at different cycles which clearly present

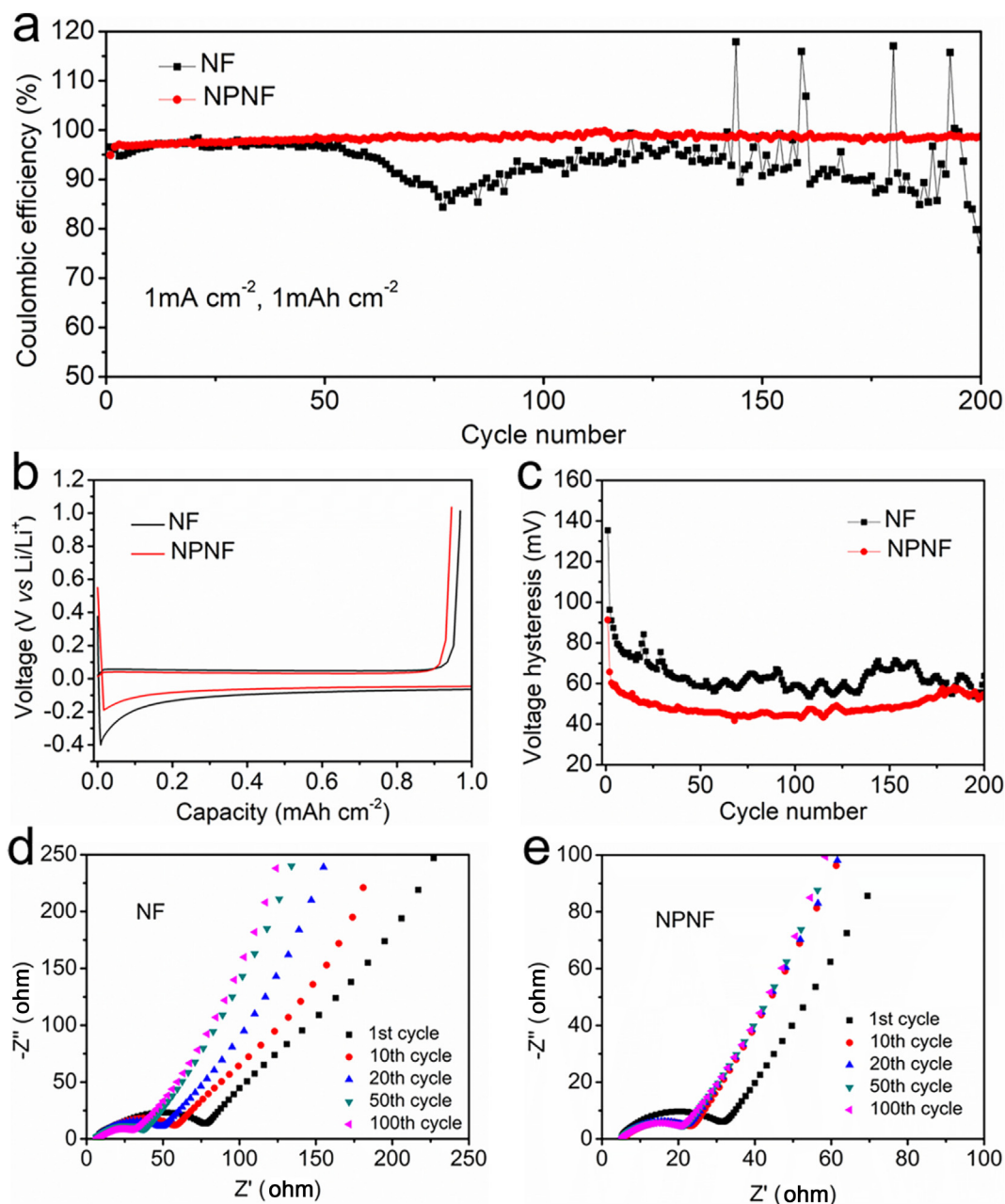


Fig. 4. (a) CE of NF and NPNF current collectors at the current density of 1 mA cm^{-2} with a capacity of 1 mAh cm^{-2} . The corresponding first voltage profiles (b) and voltage hysteresis (c) of Li plating/stripping on NF and NPNF current collectors. EIS spectra for Li plating/stripping on NF (d) and NPNF (e) current collectors after different cycles.

the lower and more stable voltage hysteresis of the NPNF current collector. In order to study the charge transfer resistance and interfacial properties, EIS test was exploited at different cycles for the both current collectors, as shown in Figs. S9 and 4(d, e). Before cycling, the NPNF current collector displays much lower charge transfer resistance and much higher ionic conductivity than those of the NF current collector (Fig. S9). This indicates that the nanopores can provide more electroactive area for the transfer of charge and Li ion between the NPNF current collector and the electrolyte. This should also be a reason for the smaller nucleation overpotential of NPNF current collector (Fig. 4b). After different cycles, the NPNF current collector remains lower charge transfer resistance than that of the NF current collector (Fig. 4d, e). Moreover, the NPNF current collector shows a stable charge transfer resistance (Fig. 4e), while the charge transfer resistance of the NF current collector decreases gradually with the increase

of cycle number (Fig. 4d). This stable charge transfer resistance indicates that there is a stable interfacial property during Li plating/stripping for NPNF current collector. The lower charge transfer resistance and stable interfacial property of the NPNF current collector further support its lower and stable voltage hysteresis. The morphology of the deposited Li metal after the 100th plating was characterized by SEM (Fig. S10). Fig. S10(a) shows obvious Li dendrite structure on the NF current collector, while the morphology of deposited Li metal on the NPNF current collector remains a flat surface (Fig. S10b).

The cycling performance of symmetrical Li||Li@NF and Li||Li@NPNF cells was investigated via galvanostatic charge and discharge at different current densities of 0.5 and 1 mA cm^{-2} with a fixed capacity of 1 mAh cm^{-1} , as shown in Fig. 5(a, b). Before cycling for 540 h, the symmetrical cell of Li||Li@NF can maintain stable cycling at 0.5 mA cm^{-2} , however the voltage of Li plating/

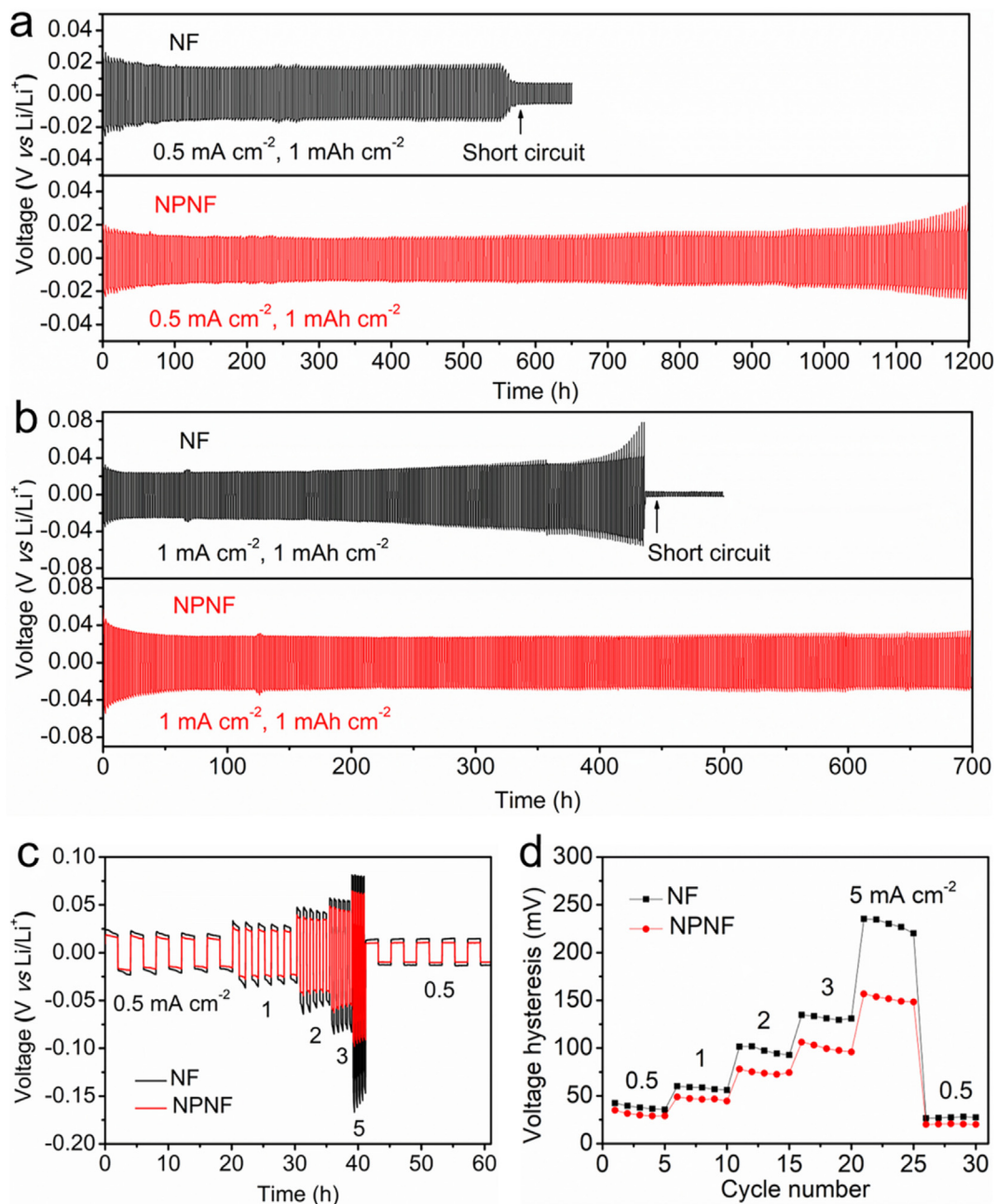


Fig. 5. Voltage-time profiles of Li plating/stripping cycles with a capacity of 1 mAh cm^{-2} at constant current densities of 0.5 mA cm^{-2} (a) and 1 mA cm^{-2} (b) and at various current densities (c) in the symmetric $\text{Li}||\text{Li@NF}$ and $\text{Li}||\text{Li@NPNF}$ cells. (d) Voltage hysteresis of Li plating/stripping process corresponding to (c).

stripping suddenly drops, indicating the occurrence of short circuit (Fig. 5a). This means that the Li dendrite has been formed and continuously grown in the symmetrical cell of $\text{Li}||\text{Li@NF}$ during cycling. In contrast, the symmetrical cell of $\text{Li}||\text{Li@NPNF}$ shows stable voltage profiles and an ultralong lifespan of 1200 h (Fig. 5a). The phenomenon of short circuit is not observed, indicating that the formation of Li dendrite has been significantly delayed owing to the reduced practical current density derived from the high surface area. When the current density increases to 1 mA cm^{-2} , the symmetrical cell of $\text{Li}||\text{Li@NF}$ also exhibits the short circuit phenomenon after cycling for 420 h (Fig. 5b). Besides, the voltage of Li plating/stripping displays a continuous increase tendency until the short circuit, which may be induced by the unstable interfacial property of Li/electrolyte interface and electrical disconnection due to the repeated growth/corrosion of Li dendrites. For the

symmetrical cell of $\text{Li}||\text{Li@NPNF}$, the Li plating/stripping process shows exceptional cycling stability with negligible voltage fluctuation for 700 h. The stable voltage profiles further indicate the stable interfacial property and the inhibition of dendritic Li formation on the Li anode based on NPNF current collector. The short circuit phenomena and voltage change can be observed distinctly from the voltage hysteresis curves (Fig. S11). The excellent cycling stability is impressive when compared to that in previous reports, as shown in Table S1. The cycling performances of symmetrical cells were further tested at a higher current density and larger cycling capacity, as shown in Fig. S12. It shows that the symmetrical cell of $\text{Li}||\text{Li@NF}$ presents much larger voltage fluctuation and voltage hysteresis and the short circuit phenomenon occurs less than 100 h. By contrast, the symmetrical cell of $\text{Li}||\text{Li@NPNF}$ presents more stable voltage behavior and smaller voltage hysteresis

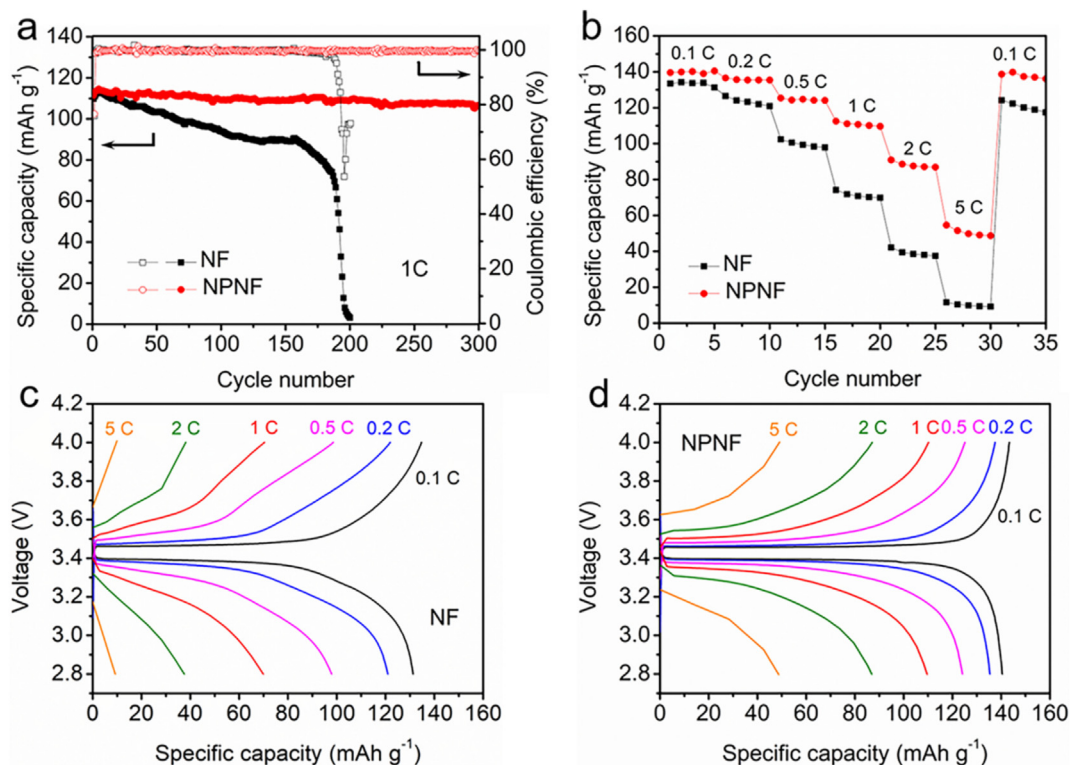


Fig. 6. Electrochemical performances of full cells of Li@NF||LFP and Li@NPNF||LFP. (a) Cycling performance at 1C, (b) rate performance and (c, d) charge–discharge curves at different rates.

and can cycle 400 h without short circuit. The SEM images in Fig. S13 show the surface morphology of Li@NPNF anodes after 20 cycles in symmetric cells at different current densities and cycling capacities. It can be observed that the Li@NPNF anodes present similar surface morphology with flat Li deposition.

In order to further investigate the voltage hysteresis behavior at different current densities, the symmetrical cell of Li||Li@NF and Li||Li@NPNF were charged and discharged for 5 cycles at each current density (0.5, 1, 2, 3, 5, 0.5 mA cm⁻²), as shown in Fig. 5(c). It shows that the symmetrical cell of Li||Li@NF has larger overpotential and voltage hysteresis than the Li||Li@NPNF cell at all current densities. This larger overpotential and voltage hysteresis of the Li||Li@NF cell should be attributed to the large internal impedance because of the accumulation of dead Li and SEI. Moreover, the difference of voltage hysteresis between the adjacent current densities is lower for the Li||Li@NPNF cell than that of the Li||Li@NF cell (Fig. 5d), which may indicate that the practical current density on the Li@NPNF anode is effectively reduced, even at high current densities, by the high surface area due to the nanopores. The detailed data about the voltage hysteresis are shown in Table S2.

The enhanced electrochemical performances of the cells based on the NPNF current collector are obviously attributed to the following features: First, the inherent macropore structure of Ni foam can partly accommodate the volume variation during Li plating/stripping. Second, the nanopores endow the NPNF current collector with high surface areas, which can reduce the local current density, hence prolong the growth of Li dendrite based on the Sand's time and reduce the voltage hysteresis. The well-distributed nanopores can also regulate the uniform lithium nucleation and deposition with homogenous distribution of Li⁺ flux. Third, the concave Li metal is spontaneously formed during both plating and stripping processes, which can guide Li metal to deposit preferentially in the interior of concave Li grains and to strip preferentially along

the rims of the concave shape, further eliminating the formation of Li dendrite [45,46].

Furthermore, full cells were assembled with the commercial LiFePO₄ (LFP) as the cathode to compare the performances of Li@NPNF and Li@NF anodes. In order to reduce the influence of cathode and to better compare the performance of anode, the cathode with low LFP mass loading was firstly applied (Fig. 6). The Li@NPNF||LFP full cell displays much better cycle stability with a high capacity retention of 93% and CE of 99.5% at 1C after 300 cycles (Fig. 6a), which demonstrates high Li utilization of the Li@NPNF anode. In contrast, the Li@NF||LFP full cell has lower specific capacity, only exhibits a capacity retention of 78.9% after 150 cycles and shows abrupt drops of the capacity and CE after 190 cycles due to the formation of dead Li during cycling, revealing low Li utilization of the Li@NF anode. Fig. 6(b) shows that the Li@NPNF||LFP full cell possesses better rate performance than the Li@NF||LFP full cell. The charge–discharge curves at different rates are shown in Fig. 6(c, d). By comparison, the Li@NPNF||LFP full cell reveals lower polarization, especially at high rate, which should be attributed to the advantages of the Li@NPNF anode, that is small local current density, stable interfacial property and low internal impedance. Then, the cathode with high LFP mass loading was applied to explore the potential of the Li@NPNF anode in practical application (Fig. S14). Fig. S14(a) shows the first three charge–discharge curves of Li@NPNF||LFP at 0.1C, and the first charge curve exhibits that the areal capacity of LFP cathode is 1.8 mAh cm⁻². The N/P ratio (areal capacity ratio of the negative and positive electrodes) is calculated to be 2.22, that is comparable to the practical cell parameter reported in the literatures [49,50]. The cycling performance tests were conducted at 0.5C after the first three cycles at 0.1C, as shown in Fig. S14(b). It can be observed that the Li@NPNF||LFP presents better cycling performance than the Li@NF||LFP, and the capacity retentions are respective 70.6% and 46.7% for the Li@NPNF||LFP and Li@NF||LFP full cells after 100 cycles.

4. Conclusions

In summary, a nanoporous Ni foam current collector with some flaws on the surface fabricated by the facile oxidation–reduction strategy is proposed for the dendrites free and highly stable LMAs. The nanopores distributed uniformly on the Ni foam skeleton endow the NPNF current collector with high surface areas, which significantly reduces the local current density, guides the homogeneous distribution of Li⁺ flux and accelerates the uniform nucleation of Li. Besides, the surface flaws induce the formation of ring structures at the initial Li nucleation/deposition processes, then the concave Li metal, spontaneously formed on the basis of the ring Li structures during cycling, can direct the Li metal to plate and strip evenly, further eliminating the formation of dendritic Li. As a result, combining with the macroporous structure of Ni foam, which can partly accommodate the volume change during Li plating/stripping, the NPNF current collector can achieve a stable CE for 200 cycles at 1 mA cm⁻² with much reduced nucleation overpotential, voltage hysteresis and more steady interface property. The symmetrical Li||Li@NPNF cells attains long lifespans of 1200 h at 0.5 mA cm⁻² and 700 h at 1 mA cm⁻² without short circuit. In addition, the Li@NPNF||LFP full cell shows excellent cycling performance at 1C for 300 cycles and rate performance with much lower polarization. The NPNF current collector is expected to reveal a synergistic effect with other feasible designs to realize its practical application in LMAs. Moreover, the nanoporous Ni foams with high surface area may also be the potential current collectors or support frameworks in the research field of supercapacitors and electrocatalysis.

Declaration of Competing Interest

The authors declare that they have no known competing financial interests or personal relationships that could have appeared to influence the work reported in this paper.

Acknowledgments

We thank the National Natural Science Foundation of China (No. 51761135123), the National Key Research & Development Program (2016YFB0303903, 2016YFE0201600).

Appendix A. Supplementary data

Supplementary data to this article can be found online at <https://doi.org/10.1016/j.jechem.2020.09.013>.

References

- [1] J.-M. Tarascon, M. Armand, *Nature* 414 (2001) 359–367.
- [2] D. Lin, Y. Liu, Y. Cui, *Nat. Nanotechnol.* 12 (2017) 194–206.
- [3] H. Zhao, D. Lei, Y.-B. He, Y. Yuan, Q. Yun, B. Ni, W. Lv, B. Li, Q.-H. Yang, F. Kang, J. Lu, *Adv. Energy Mater.* 8 (2018) 1800266.
- [4] R. Wang, W. Cui, F. Chu, F. Wu, *J. Energy Chem.* 48 (2020) 145–159.
- [5] X. Liu, D. Chao, D. Su, S. Liu, L. Chen, C. Chi, J. Lin, Z.X. Shen, J. Zhao, L. Mai, Y. Li, *Nano Energy* 37 (2017) 108–117.
- [6] W. Xu, J. Wang, F. Ding, X. Chen, E. Nasybulin, Y. Zhang, J.-G. Zhang, *Energy Environ. Sci.* 7 (2014) 513–537.
- [7] X. Shen, X. Cheng, P. Shi, J. Huang, X. Zhang, C. Yan, T. Li, Q. Zhang, *J. Energy Chem.* 37 (2019) 29–34.
- [8] Y. Zhang, T.-T. Zuo, J. Popovic, K. Lim, Y.-X. Yin, J. Maier, Y.-G. Guo, *Mater. Today* 33 (2020) 56–74.
- [9] X.-B. Cheng, R. Zhang, C.-Z. Zhao, Q. Zhang, *Chem. Rev.* 117 (2017) 10403–10473.
- [10] X. Xu, S. Wang, H. Wang, C. Hu, Y. Jin, J. Liu, H. Yan, *J. Energy Chem.* 27 (2018) 513–527.
- [11] X. Ke, Y. Liang, L. Ou, H. Liu, Y. Chen, W. Wu, Y. Cheng, Z. Guo, Y. Lai, P. Liu, Z. Shi, *Energy Storage Mater.* 23 (2019) 547–555.
- [12] H. Qiu, T. Tang, M. Asif, X. Huang, Y. Hou, *Adv. Funct. Mater.* 29 (2019) 1808468.
- [13] Y. Guo, H. Li, T. Zhai, *Adv. Mater.* 29 (2017) 1700007.
- [14] Y. Chen, Y. Luo, H. Zhang, C. Qu, H. Zhang, X. Li, *Small Methods* 3 (2019) 1800551.
- [15] F. Wu, Y.-X. Yuan, X.-B. Cheng, Y. Bai, Y. Li, C. Wu, Q. Zhang, *Energy Storage Mater.* 15 (2018) 148–170.
- [16] Y. Nan, S. Li, Y. Shi, S. Yang, B. Li, *Small* 15 (2019) 1903520.
- [17] Y. Shi, Z. Wang, H. Gao, J. Niu, W. Ma, J. Qin, Z. Peng, Z. Zhang, *J. Mater. Chem. A* 7 (2019) 1092–1098.
- [18] R. Song, B. Wang, Y. Xie, T. Ruan, F. Wang, Y. Yuan, D. Wang, S. Dou, *J. Mater. Chem. A* 6 (2018) 17967–17976.
- [19] X.-Q. Zhang, X.-B. Cheng, X. Chen, C. Yan, Q. Zhang, *Adv. Funct. Mater.* 27 (2017) 1605989.
- [20] H. Ota, K. Shima, M. Ue, J.-I. Yamaki, *Electrochim. Acta* 49 (2004) 565–572.
- [21] H. Ye, Y.-X. Yin, S.-F. Zhang, Y. Shi, L. Liu, X.-X. Zeng, R. Wen, Y.-G. Guo, L.-J. Wan, *Nano Energy* 36 (2017) 411–417.
- [22] W. Li, H. Yao, K. Yan, G. Zheng, Z. Liang, Y.-M. Chiang, Y. Cui, *Nat. Commun.* 6 (2015) 7436–7443.
- [23] Y. Liu, D. Lin, Z. Liang, J. Zhao, K. Yan, Y. Cui, *Nat. Commun.* 7 (2016) 10992–11000.
- [24] G. Zheng, S.W. Lee, Z. Liang, H.-W. Lee, K. Yan, H. Yao, H. Wang, W. Li, S. Chu, Y. Cui, *Nat. Nanotechnol.* 9 (2014) 618–623.
- [25] N.-W. Li, Y.-X. Yin, C.-P. Yang, Y.-G. Guo, *Adv. Mater.* 28 (2016) 1853–1858.
- [26] Y. Yuan, F. Wu, G. Chen, Y. Bai, C. Wu, *J. Energy Chem.* 37 (2019) 197–203.
- [27] X.-B. Cheng, R. Zhang, C.-Z. Zhao, F. Wei, J.-G. Zhang, Q. Zhang, *Adv. Sci.* 3 (2016) 1500213.
- [28] W. Wang, C. Liao, K.M. Liew, Z. Chen, L. Song, Y. Kan, Y. Hu, *J. Mater. Chem. A* 7 (2019) 6859–6868.
- [29] L. Nie, Y. Li, S. Chen, K. Li, Y. Huang, Y. Zhu, Z. Sun, J. Zhang, Y. He, M. Cui, S. Wei, F. Qiu, C. Zhong, W. Liu, *ACS Appl. Mater. Interfaces* 11 (2019) 32373–32380.
- [30] P.J. Kim, V.G. Pol, *Adv. Energy Mater.* 8 (2018) 1802665.
- [31] H. Liu, E. Wang, Q. Zhang, Y. Ren, X. Guo, L. Wang, G. Li, H. Yu, *Energy Storage Mater.* 17 (2019) 253–259.
- [32] Y. An, H. Fei, G. Zeng, X. Xu, L. Ci, B. Xi, S. Xiong, J. Feng, Y. Qian, *Nano Energy* 47 (2018) 503–511.
- [33] Q. Yun, Y.-B. He, W. Lv, Y. Zhao, B. Li, F. Kang, Q.-H. Yang, *Adv. Mater.* 28 (2016) 6932–6939.
- [34] S.-H. Wang, Y.-X. Yin, T.-T. Zuo, W. Dong, J.-Y. Li, J.-L. Shi, C.-H. Zhang, N.-W. Li, C.-J. Li, Y.-G. Guo, *Adv. Mater.* 29 (2017) 1703729.
- [35] X. Ke, Y. Cheng, J. Liu, L. Liu, N. Wang, J. Liu, C. Chi, Z. Shi, Z. Guo, *ACS Appl. Mater. Interfaces* 10 (2018) 13552–13561.
- [36] Y. Xu, A.S. Menon, P.P.R.M.L. Harks, D.C. Hermes, L.A. Haverkate, S. Unnikrishnan, F.M. Mulder, *Energy Storage Mater.* 12 (2018) 69–78.
- [37] L. Kong, Q. Zhang, *J. Energy Chem.* 33 (2019) 167–168.
- [38] L. Liu, Y.-X. Yin, J.-Y. Li, S.-H. Wang, Y.-G. Guo, L.-J. Wan, *Adv. Mater.* 30 (2018) 1706216.
- [39] X. Zhang, A. Wang, X. Liu, J. Luo, *Acc. Chem. Res.* 52 (2019) 3223–3232.
- [40] S. Liu, X. Liu, J. Zhao, Z. Tong, J. Wang, X. Ma, C. Chi, D. Su, X. Liu, Y. Li, *RSC Adv.* 6 (2016) 85222–85229.
- [41] J. Wang, X. Zhang, Q. Wei, H. Lv, Y. Tian, Z. Tong, X. Liu, J. Hao, H. Qu, J. Zhao, Y. Li, L. Mai, *Nano Energy* 19 (2016) 222–233.
- [42] W. Xi, G. Yan, Z. Lang, Y. Ma, H. Tan, H. Zhu, Y. Wang, Y. Li, *Small* 14 (2018) 1802204.
- [43] K. Yan, Z. Lu, H.-W. Lee, F. Xiong, P.-C. Hsu, Y. Li, J. Zhao, S. Chu, Y. Cui, *Nat. Energy* 1 (2016) 16010.
- [44] S.-S. Chi, Y. Liu, W.-L. Song, L.-Z. Fan, Q. Zhang, *Adv. Funct. Mater.* 27 (2017) 1700348.
- [45] J. Ahn, J. Park, J.Y. Kim, S. Yoon, Y.M. Lee, S. Hong, Y.-G. Lee, C. Phatak, K.Y. Cho, *ACS Appl. Energy Mater.* 2 (2019) 5656–5664.
- [46] M.-H. Ryou, Y.M. Lee, Y. Lee, M. Winter, P. Bieker, *Adv. Funct. Mater.* 25 (2015) 834–841.
- [47] Y. Li, J. Jiao, J. Bi, X. Wang, Z. Wang, L. Chen, *Nano Energy* 32 (2017) 241–246.
- [48] J. Gu, Q. Zhu, Y. Shi, H. Chen, D. Zhang, Z. Du, S. Yang, *ACS Nano* 14 (2020) 891–898.
- [49] H. Li, *Joule* 3 (2019) 911–914.
- [50] S. Chen, C. Niu, H. Lee, Q. Li, L. Yu, W. Xu, J.-G. Zhang, E.J. Dufek, M.S. Whittingham, S. Meng, J. Xiao, J. Liu, *Joule* 3 (2019) 1–12.